Optica Applicata, Vol. XL, No. 4, 2010

A geometry and optical property inspection system for automotive glass based on fringe patterns

JING XU[1*], NING XI[1], CHI ZHANG[1], QUAN SHI[2], JOHN GREGORY[1]

[1]Electrical and Computer Engineering Department, Michigan State University, East Lansing, MI, 48824, USA

[2]PPG Industries Inc., Glass Research Center, 400 Guys Run Road, Cheswick, PA, 15024, USA

[*]Corresponding author: xujing0829@gmail.com

In this paper, an automotive glass inspection system based on fringe patterns is proposed. This system can inspect the 3D shape, reflection normal and transmission distortion of the automotive glass simultaneously. A stereo vision and an iterative algorithm based on the reflection law of the specular surface are utilized to obtain the 3D shape and reflection normal of the inspected part. Then, the bottom reflection of the glass is analyzed such that the line-shifting fringe pattern, based on step wave, is adopted. Additionally, the transmission distortion is defined as an angle between the incoming ray and the outgoing ray for the inspected automotive glass. The method proposed is simpler and more flexible than traditional methods. Finally, the system accuracy has been examined, with the results demonstrating its high accurate performance.

Keywords: specular surface, quality inspection, transmission distortion.

1. Introduction

In automotive glass manufacturing industry, the 3D shape and optical property are the most important specifications of the glass, which influence the glass installation, the efficiency of windshield wiper, and the security of the driver. Thus, there has been an increasing requirement for fast measurement of the 3D shape of the automotive glass for manufacturing quality inspection by using innovative noncontact vision--based 3D area sensors [1]. Compared with traditional coordinate measurement machine (CMM) technique, it has the advantages of high point density and rapid measurement speed. However, the biggest challenges for direct measurement of the transparent glass are that the light reflected by the specular surface travels through in one direction, and the bottom reflection of transparent glass affects the decoding of fringe patterns. The first challenge does not allow us to directly apply the vision-based measurement technique used for diffuse part inspection. Additionally, the bottom reflection affects the inspection accuracy. Therefore, for quality inspection, the specular surface should be modified, *e.g.*, coated with non-reflective material [2]. This operation will reduce the inspection accuracy and decrease the speed.

Some attempts have been made for specular part inspection. The 3D shape of the specular surface can be obtained through the movement of the light source or camera. The drawback of such method is low measurement speed since each point of the scene needs to be analyzed at different angles [3]. To overcome this limitation, a diffuse screen is adopted as a structured light source, and then the entire finger pattern reflected by the specular surface can be observed by the camera simultaneously. By analyzing the phase distribution of the fringe patterns, a relation between the surface slope and position can be obtained such that the 3D shape of the specular surface can be calculated by local integration. However, the random noise will accumulate and cause error propagation [4]. To overcome such limitation, the global integration algorithm is proposed [5]. An alternative way to acquire the 3D shape of the specular part is to move the diffuse light source to two different locations. The corresponding phase distributions of the pixel in the light source are obtained such that the incident ray for the specular surface point can be calculated. Combining the reflected ray obtained by camera calibration, the 3D shape of the specular part can be constructed [6].

The transmission distortion inspection of the automotive glass is a security relevant issue, especially for the windshield. The transmission distortion is defined as the optical ray deviation through the automotive glass, resulting in the distortion of the observed scene. The transmission distortion arises from many sources, such as thickness variation, and spatial frequency as well. Some techniques are developed for transmission distortion inspection [7]. The moiré interferometry is used for the inspection of spot windshield defects [8].

In this paper, an integrated vision-based inspection system for 3D shape, reflection normal and transmission distortion of the automotive glass has been proposed. The stereo cameras in this system are utilized for 3D shape and reflection normal measurement and another single camera is used for transmission distortion inspection.

The remaining part of this paper is arranged as follows: the principle, fringe pattern and calibration are given in Section 2; In Section 3, the accuracy experiments and results are introduced; the conclusion is given in Section 4.

2. Theory

The inspection of 3D shape and reflection normal by stereo vision is proposed in Section 2.1. Based on the top surface shape and transmitted light rays of the transparent glass, the transmission distortion is measured in Section 2.2. In Section 2.3, the bottom reflection is analyzed to correctly decode the fringe patterns shot onto the transparent glass. The prerequisite of the accurate measurement is to calibrate components and inspection system; thus, calibration is described in Section 2.4.

2.1. Stereo vision for 3D shape and reflection normal inspection

A point light source cannot be used to inspect the automotive glass because the incident light ray is reflected in one direction only. Hence, a diffuse light source is required to provide the incoming light from many directions so that the reflected rays can be

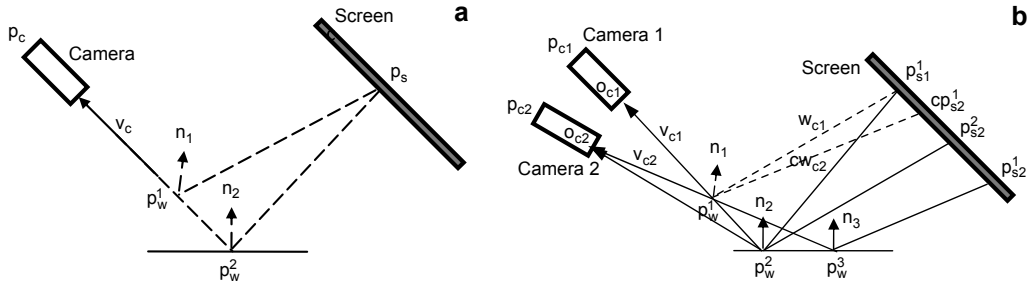

Fig. 1. Measure automotive glass using diffuse planar light source: single camera (**a**); stereo vision (**b**).

observed by the camera. In our system, it is implemented by projecting the fringe patterns to the screen (a white board) using a projector, and then the screen is considered as a diffuse light source [10]. However, a single camera arrangement cannot satisfy the requirement of triangulation-based inspection technique because there are two groups of unknown parameters: the normal and position. The position determination depends on the normal, *e.g.*, n_1 corresponds to p_w^1 while n_2 corresponds to p_w^2 in Fig. 1**a**.

To clarify the ambiguity, another camera has been introduced as shown in Fig. 1**b**. To use the stereo vision technique, the correspondence problem must be solved in advance. The challenge for this system is that the correspondence match based on the decoding of fringe pattern will fail because the points on the automotive glass reflecting the same phase in the screen probably are not the same point on the glass surface. Luckily, the normal and the reflection law can be used to solve the correspondence problem by iterative search algorithm. A detailed measurement procedure is described as follows.

In Figure 1**b**, camera 1 is selected as the primary camera while camera 2 is the secondary camera. For each pixel in the primary camera, we need to find a corresponding pixel in the secondary camera by iterative search algorithm. The iterative procedure is described as follows: given the corresponding pixel p_{c2} in camera image I_2 for the point p_{c1} in the camera image I_1, the corresponding intersection p_w^1 is determined by triangulation measurement technique as shown in Fig. 1**b**. Combining the reflected ray vector v_{c1} and incident raster point p_{s1}^1 on the screen, the normal vector n_1 between the incident ray vector w_{c1} and the reflected ray vector v_{c1} is calculated from camera 1. The normal vector n_1 is also the normal for camera 2. Hence, for camera 2, taking into account the normal vector n_1 and the reflected ray vector v_{c2}, the "calculated" incident vector cw_{c2} can be represented by

$$cw_{c2} = v_{c2} - 2\frac{n_1 v_{c2}}{|n_1|^2} n_1 \tag{1}$$

Then, the "calculated" intersection point cp_{s2}^1 between this vector and the screen can be computed. Actually, the "real" point is the observed point p_{s2}^1 for camera 2.

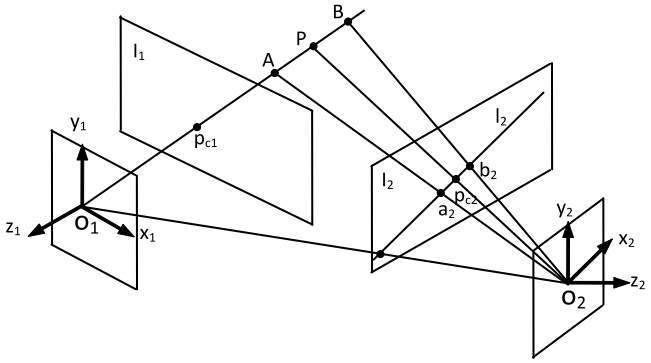

Fig. 2. Epipolar geometry constraint.

If the assumed pixel p_{c2} in image I_2 is the real corresponding pixel for the pixel p_{c1} in image I_1, then the "real" point p_{s2}^1 and the "calculated" point cp_{s2}^1 coincide. Therefore, the difference between these two raster points is our searching criterion. Thus, the iterative algorithm is performed by minimizing the distance between the "real" point and the "calculated" point on the screen for camera 2.

Once the above correspondence problem has been solved, the position and the normal of the automotive glass surface can be further determined. A similar method called "stereo deflectometry" for measuring the specular surface was proposed in [9, 10].

In order to improve the searching speed performance, some constraints are introduced as follows.

The epipolar geometry in stereo vision is utilized as the first constraint. Consider the case shown in Fig. 2, where P is a point on the surface of automotive glass; p_{c1} and p_{c2} are the projections of the point P on the camera image plane I_1 and I_2, respectively. The epipolar line in image I_2 can be represented by l_2. Thus, for point p_{c2}, the corresponding point of p_{c1}, is constricted to lie on the epipolar line l_2. Recall that

$$l_2 = F p_{c1} \tag{2}$$

where F is the fundamental matrix determined by calibration [11]. Hence, the correspondence problem is reduced from 2D search (the whole image) to 1D search problem (along the epipolar line).

The CAD model is used as the second constraint. Since the real part surface is actually very close to the standard CAD model during the manufacturing procedure, the corresponding pixel p_{c2} in image I_2 can be further constrained into a small segment along the epipolar line according to a user-defined error threshold, *e.g.*, the segment $a_2 b_2$ as shown in Fig. 2.

Now, we will analyze whether any other assumed pixel satisfies the criterion proposed in the neighborhood of the real corresponding pixel in camera 2. Consider

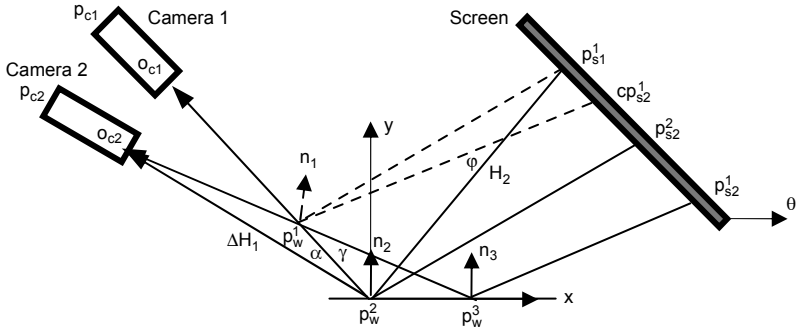

Fig. 3. Parameters for stereo vision: the angle between the two viewing vectors through the optical center o_{c2} in camera 2 is defined as $\angle p_w^1 o_{c2} p_w^2 = \Delta$; the angle between the two viewing vectors for camera 1 and camera 2 at real position p_w^2 is defined as $\angle o_{c2} p_w^2 o_{c1} = \alpha$; the angle between the two assumed positions for the point p_{s1}^1 is defined as $\angle p_w^2 p_{s1}^1 p_w^1 = \varphi$; the incident and reflected angles at point p_w^2 are defined as γ, the length of the viewing vector and the incident vector for camera 2 are defined as $o_{c2} p_w^2 = H_1$, $\angle p_w^2 p_{s1}^1 = H_2$, respectively; the local coordinate frame is established at the point p_w^2. The slope angle of the screen is defined as θ. The coordinates of points p_w^1, p_w^3 and p_{s1}^1 are $p_w^1 = [-H_1 \csc(\alpha+\Delta)\sin(\gamma)\sin(\Delta) - H_1 \cos(\gamma)\csc(\alpha+\Delta)\sin(\Delta)]$, $p_w^3 = [H_1 \sec(\alpha+\Delta+\gamma)\sin(\Delta) \quad 0]$, $p_{s1}^1 = [H_2 \sin(\gamma) \quad H_2 \cos(\gamma)]$.

the two dimensional case of the procedure as shown in Fig. 1**b**, where point p_w^2 is the real point and p_w^1 is the incorrectly assumed point above the real one.

Based on the geometry property and reflection law, we can determine a slope angle of the real incident vector $p_w^3 p_{s2}^1$ and the calculated incident vector $p_w^1 c p_{s2}^1$ as $(\pi/2 - \gamma - \Delta - \alpha)$, $(\pi/2 - \varphi - \gamma - \Delta - \alpha)$, respectively.

During the iterative searching, angle Δ is the only variable. The objective is to find out the relationship between the angle Δ and the criterion function used in this paper.

Based on the sine law in the triangle $\Delta p_w^1 p_w^2 o_{c2}$ and $\Delta p_w^1 p_w^2 p_w^3$, the length of $p_w^1 p_w^2$ and $p_w^2 p_w^3$ can be represented as:

$$p_w^1 p_w^2 = H_1 \frac{\sin(\Delta)}{\sin(\Delta+\alpha)} \quad p_w^2 p_w^3 = H_1 \frac{\sin(\Delta)}{\cos(\alpha+\Delta+\gamma)} \tag{3}$$

Similarly, in triangle $\Delta p_w^1 p_w^2 p_w^3$, the angle φ can be denoted by

$$\varphi = a\tan\left(\frac{A\sin(2\gamma)}{H_2 - A\cos(2\gamma)}\right) \tag{4}$$

For small angles, $\tan(\Delta) \approx \Delta$, so that Eq. (4) can be rewritten as

$$\varphi = \frac{H_1 \csc(\alpha)\sin(2\gamma)}{H_2}\Delta \tag{5}$$

The x coordinate of the point cp_{s2}^1 can be obtained by the intersection of $p_w^1 c p_{s2}^1$ on the screen

$$x_1 = \cos(\gamma)\left[H_2 - H_1\csc(\alpha+\Delta)\sin(\Delta) - \sin(r)\right]\times$$

$$\times \frac{H_1\cot(\alpha+\gamma+\Delta+\varphi)\csc(\alpha+\Delta)\sin(\Delta) + H_2\tan(\theta)}{\cot(\alpha+\gamma+\Delta+\varphi) - \tan(\theta)} \tag{6}$$

Similarly, the x coordinate of the point p_{s2}^1 can be obtained by the intersection of $p_w^2 p_{s2}^1$ on the screen

$$x_2 = \frac{H_2\cos(\gamma) + H_1\csc(\alpha+\gamma+\Delta)\sin(\Delta) - H_2\sin(\gamma)\tan(\theta)}{\cot(\alpha+\gamma+\Delta) - \tan(\theta)} \tag{7}$$

The difference between point p_{s2}^1 and point cp_{s2}^1 in axis x can be expressed as

$$f(\Delta) = x_1 - x_2 \tag{8}$$

It can be expanded around $\Delta = 0$ with the first order Taylor series expansion

$$f(\Delta) \approx f(0) + f'(0)\Delta \tag{9}$$

where $f'(0) = -2H_1\cos(\gamma)\cos(\theta)\cos(\alpha+2\gamma+\theta)\sec^2(\alpha+\gamma+\theta)$.

From Equation (9), it is found that if $f'(0) > 0$ or $f'(0) < 0$, then the solution is unique. Fortunately, with the automotive glass, the slope changes slightly and the searching range is in the neighborhood of the CAD mode; thus, it is easy to guarantee the requirement.

2.2. Transmission distortion inspection

The basic principle for transmission distortion inspection is shown in Fig. 4. When there is no automotive glass installed in the inspection system, the camera will observe the raster point A with the phase value φ_1 on the screen, with the light ray being a straight line. Once the automotive glass is installed in our system, the observed raster point on the screen will change to point A′ with phase value φ_2. In this case, the light ray is curved due to the automotive glass. The angle $\angle$AMA′ (α) between the two rays that were parallel before the transmission through the automotive glass is defined as

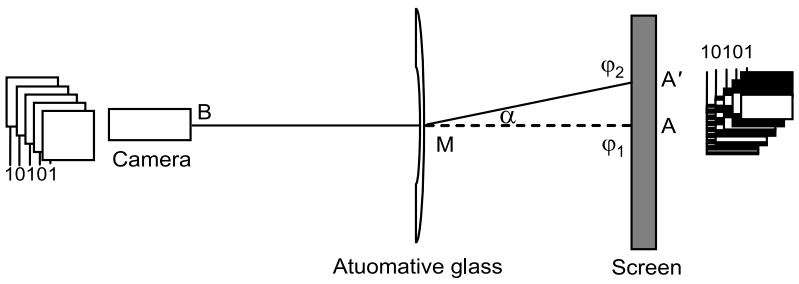

Fig. 4. Transmission distortion measurement principle.

the transmission distortion. Since the shape of the automotive glass is determined by the stereo vision inspection system, the length of AM and A′M is easily determined. Therefore, the angle of transmission distortion for point M on the automotive glass surface is represented as

$$\alpha = \arccos\left(\frac{\mathrm{AM}^2 + \mathrm{A'M}^2 - \mathrm{A'A}^2}{2\mathrm{AM} \cdot \mathrm{A'M}}\right) \tag{10}$$

where AA′ is the distance between point A and point A′ on the screen, which can be determined by screen calibration.

2.3. Fringe patterns

Both the geometry and optical property inspection need an appropriate fringe pattern to increase the measurement accuracy. Hence, we will discuss the pattern in this subsection.

During the measurement procedure, reflection and refraction phenomena will occur simultaneously when a light ray reaches the interface between the glass and the air as shown in Fig. 5**a**. A portion of the light will be transmitted while the other portion will be reflected back by the bottom layer of the glass and refracted to the air again. Thus, the reflected rays on the top layer can be divided into two categories: the top reflection and the bottom reflection. Figure 5**b** illustrates one captured image reflected by the automotive glass using a line-shifting pattern. The intensity of the bottom reflection is lower than that of top reflection.

The combination of gray code and phase shifting (GCPS) is usually recognized as an efficient technique that allows automated fringe patterns processing and analysis [12]. Due to the bottom reflection and the continuous nonlinear signal property of the sinusoidal wave, the intensity is a combination of the bottom and top reflection. In this case, the pulse wave will have superior performance over the sinuous wave because the bottom layer reflection and the top layer reflection can be separated. In this paper, the combination of gray code and line shifting (GCLS), the peak (ridge) of pulse wave is adopted instead of the GCPS.

For the line shifting, precise determination of the peak (ridge) of the line is critical for a successful 3D shape measurement. First, the bottom layer reflection is filtered

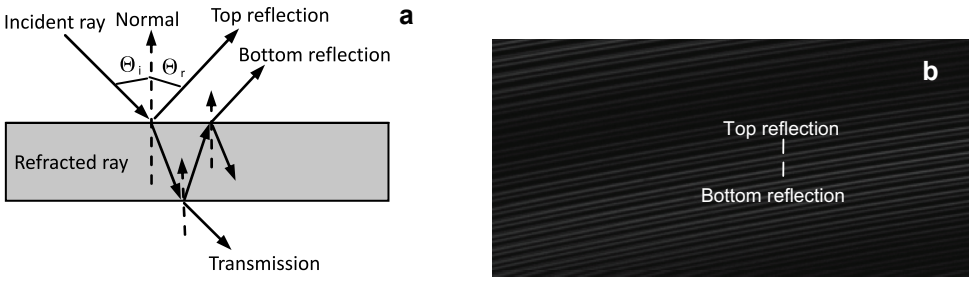

Fig. 5. Bottom layer reflection: theoretical analysis (**a**), experimental image (**b**).

out according to a given threshold. Then, the peak of the fringe pattern from the top reflection can be detected by the fourth order linear filter proposed by FISHER and NAIDU [13]

$$g_4(x) = f(x-2) + f(x-1) - f(x+1) - f(x+2) \tag{11}$$

The algorithm is operated as a numerical derivative operator in the perpendicular direction of the shifted line. Then the peak of the fringe is

$$\delta = \frac{g(x)}{g(x) - g(x+1)} \tag{12}$$

Note that such an operator is only used for the situation where $f(x+1) > f(x-1)$. If $f(x+1) < f(x-1)$, then, the peak of fringe can be determined by:

$$\delta = \frac{g(x-1)}{g(x-1) - g(x)} - 1 \tag{13}$$

A subpixel accuracy can be achieved by the above algorithm. The stripe value of the gray code can be determined using predefined threshold and the boundary of the stripe probably has an error ±1. However, it can be removed with the help of accurate coding of line shifting because the combined values of gray code and line shifting should be ascendant.

To determine the pixel location on the screen, the phase value φ should be obtained in both horizontal and vertical direction. We have to project horizontal and vertical fringes to detect the position in both directions. Figure 6 demonstrates a combination of gray code and line shifting in the horizontal direction, which generates 24 codes.

The resolution of our screen is 1024×768 pixels. In practice, six patterns are used to produce 64 vertical stripes so that each stripe has 16 pixels. Then each stripe is shifted 16 times to generate 64×16 codes. Likewise, six patterns are used to produce 64 horizontal stripes, so that each stripe has 12 pixels; each stripe should be shifted 12 times to generate 64×12 = 768 codes.

The drawback of the GCLS method is that it needs more images than GCPS method to obtain required point density, which will slow down the measurement process. However, for inspection, the measurement accuracy and measurement precision are

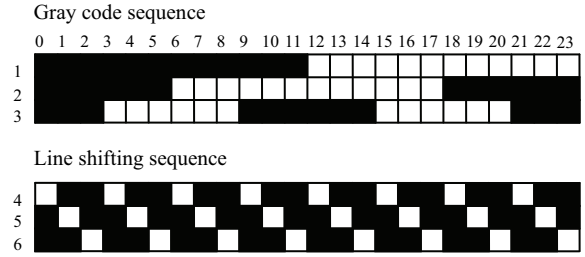

Fig. 6. Combination of gray code and line shifting.

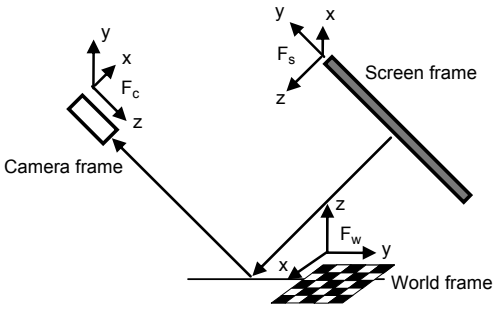

Fig. 7. Coordinate frames in area sensor.

more important. Hence, the GCLS method is adopted in this paper for the inspection system developed.

2.4. Calibration

In the inspection system, there are three types of coordinate: a camera, a screen and a world coordinate frame, as shown in Fig. 7. The objective of calibration is to transform the camera and the screen coordinate frames into the world coordinate frame. Since the calibration procedures of the three cameras are similar, only one camera calibration is described in this paper.

The calibration procedure can be divided into four steps: 1) camera calibration, 2) camera-to-world coordinate frame calibration, 3) screen calibration, 4) screen-to--world coordinate frame calibration.

First, the camera calibration is to obtain the intrinsic parameters. A camera is regarded as a pinhole model in our system. A piece of flat glass with checkerboard (15×15 mm) on it is regarded as a calibration gauge. Then the gauge placed at different positions and orientations are scanned by the camera shown in Fig. 7. We calibrate the camera using Zhang's method [14].

Second, a uniform world frame for three cameras is established with its *xy* axes located on one of the calibration checkerboard planes and the *z* axis perpendicular to this plane, as shown in Fig. 7. This world frame is defined as the world frame of the whole system.

Third, the index coordinate (r, c) of the pixel on the screen is the same coordinate in the projector. This coordinate should be converted into physical coordinate (x_s, y_s) (unit: mm) in the screen frame F_c, as shown in Fig. 7. The objective of the screen calibration is to find a homography matrix f satisfying

$$\begin{pmatrix} x_s \\ y_s \end{pmatrix} = f \begin{pmatrix} r \\ c \end{pmatrix} \tag{14}$$

For this purpose, a thin plate with n precise holes with coordinate (x_s, y_s) is covered on the screen. We can measure the corresponding index coordinates (r, c) for each hole. Next, homography matrix f can be determined by the least square method.

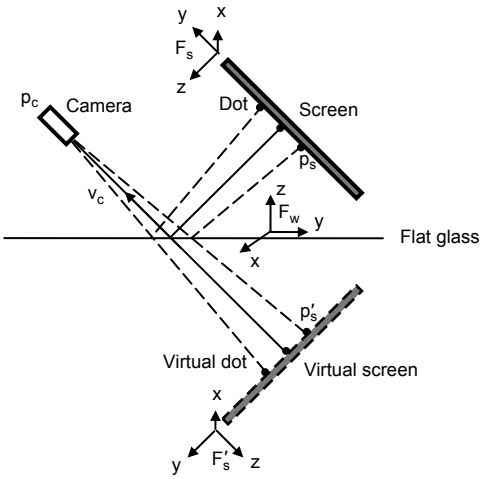

Fig. 8. Virtual image of the screen.

Last, in order to obtain the transformation matrix ${}^{w}T_{s}$ from the screen-to-world coordinate frame, another flat glass with the same geometry as the one used in camera calibration has been introduced. The glass is placed such that its top surface coincides with the *xy* plane of the uniform world frame. The coordinate frames of the screen and virtual screen are defined as shown in Fig. 8. The virtual screen is first calibrated due to the absence of the screen in the view field of the camera.

The screen generates a series of dots, whose coordinates in the screen frame can be obtained. Let p_s^i denote the coordinate of the *i*-th dot in the screen frame F_s and $p_{s'}^i$ denote the coordinate of the *i*-th virtual dot in the virtual screen frame $F_{s'}$. We have the relation that $p_s^i = p_{s'}^i$ because the magnitude is zero in the *z* direction.

Let p_w^i denote the coordinate of the *i*-th virtual dot in the world frame; then, it can be represented by:

$$p_w^i = {}^{w}T_{s'}\, p_{s'}^i, \tag{15}$$

where ${}^{w}T_{s'}$ is the transformation matrix from virtual screen to world frame.

The view vector v_w^i in the world coordinate frame corresponding to the *i*-th virtual dot p_w^i can be identified due to camera calibration. Let d_i denote the distance from the virtual dot p_w^i to the view vector v_w^i; then, the matrix ${}^{c}T_{w}$ can be identified by minimizing

$$\sum_{i=1}^{n} \left\| d_i d_i^T \right\| = \sum_{i=1}^{n} \left\| \left(v_w^i \times {}^{w}T_{s'}\, p_{s'}^i \right) \left(v_w^i \times {}^{w}T_{s'}\, p_{s'}^i \right)^T \right\| \tag{16}$$

Once the transformation matrix from the virtual screen to the world frame has been identified, the coordinate of the virtual dot in the world frame can be determined by Eq. (8). Actually, the dot and virtual dot have the same coordinate in the world

frame except the changed sign in the z direction. Therefore, the dot coordinate ${}^{*}p_i^w$ in the world frame can be determined by [10]

$$ {}^{*}p_i^w = f(p_w^i) = \begin{bmatrix} p_{wx} & p_{wy} & -p_{wz} \end{bmatrix}^T \tag{17} $$

Then, the transformation matrix ${}^{w}T_s$ from the screen to the world frame can be obtained by minimizing

$$ \sum_{i=1}^{n} \left\| {}^{*}p_i^w - {}^{w}T_s p_s^i \right\|^2 \tag{18} $$

3. Experiments and results

The system setup is constructed with aluminium T slots. The measurement components consist of three cameras (SONY XCD X 710 with FUJINON TV LENS), one projector (PLUS V339), one board, serving as diffuse screen, and one computer with frame grabber. The computer generates the fringe patterns and sends them to the projector; the projector shoots the fringe patterns to the diffuse screen. Then, the top stereo cameras observe the distorted fringe patterns reflected by the automotive glass for 3D shape inspection; the bottom camera captures the distorted fringe patterns transmitted by the automotive glass for transmission distortion inspection as shown in Fig. 9. The size of inspected glass can reach around 450×450 mm. Multiple groups of sensors can be used for larger glass as in [2].

The first experiment is carried out to verify the accuracy of the inspection system. For this purpose, a piece of flat planar glass is introduced and inspected by the system. Then the measured point cloud is fitted to an ideal plane using the linear square method,

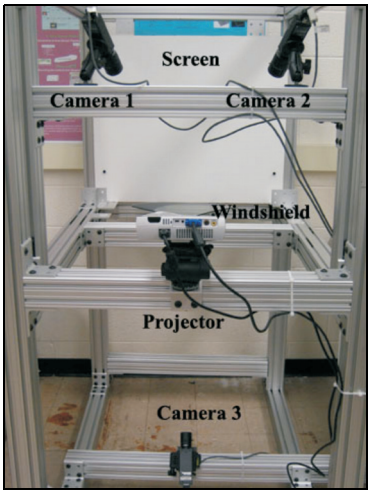

Fig. 9. Experimental phantom.

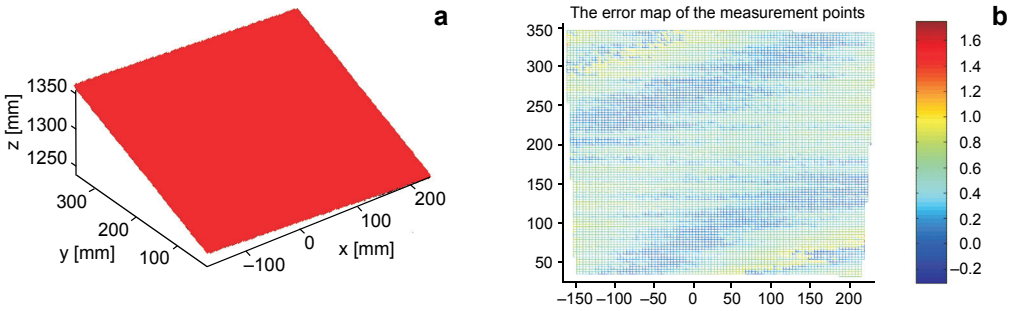

Fig. 10. The measured flat glass: fitted plan (**a**), the error of measured point (**b**).

as shown in Fig. 10**a**. The distance between the measured point and the fitted plane is the error for the measured point, as shown in Fig. 10**b**. The mean error and standard deviation of the inspection system are 0.25 mm and 0.22 mm, respectively. It should be pointed out that the accuracy of the inspection system is related to the length of the baseline between the two camera optical centers (the longer the length, the higher the accuracy), the vision depth (the shorter the depth, the higher the accuracy). However, the longer length and shorter depth will reduce the field of view for the inspection system.

The second experiment is conducted to inspect the automotive glass. Figure 11**a** shows the inspected automotive glass; the corresponding CAD model, including 576 triangles, is illustrated as in Fig. 11**b**.

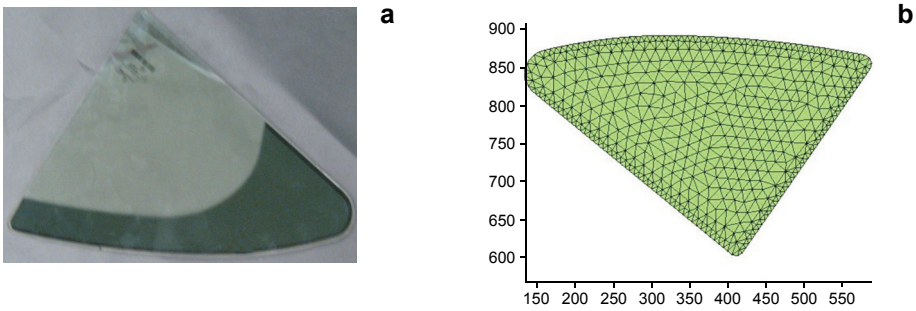

Fig. 11. The inspected automotive glass: physical glass (**a**), CAD model (**b**).

In order to measure the transmission distortion of the automotive glass, the phase distribution of the view field in the absence of the automotive glass is first determined as the reference phase distribution. Next, the automotive glass is installed in our system. The automotive glass is measured by the top stereo cameras to obtain a point cloud as shown in Fig. 12**a**. Then, it is registered with the CAD model by iterative closed point (ICP) algorithm and generates the color-code error map as shown in Fig. 12**b**. The error map shows the deviation of the measured point cloud and its CAD model for quality inspection. Additionally, the surface normal of the automotive glass

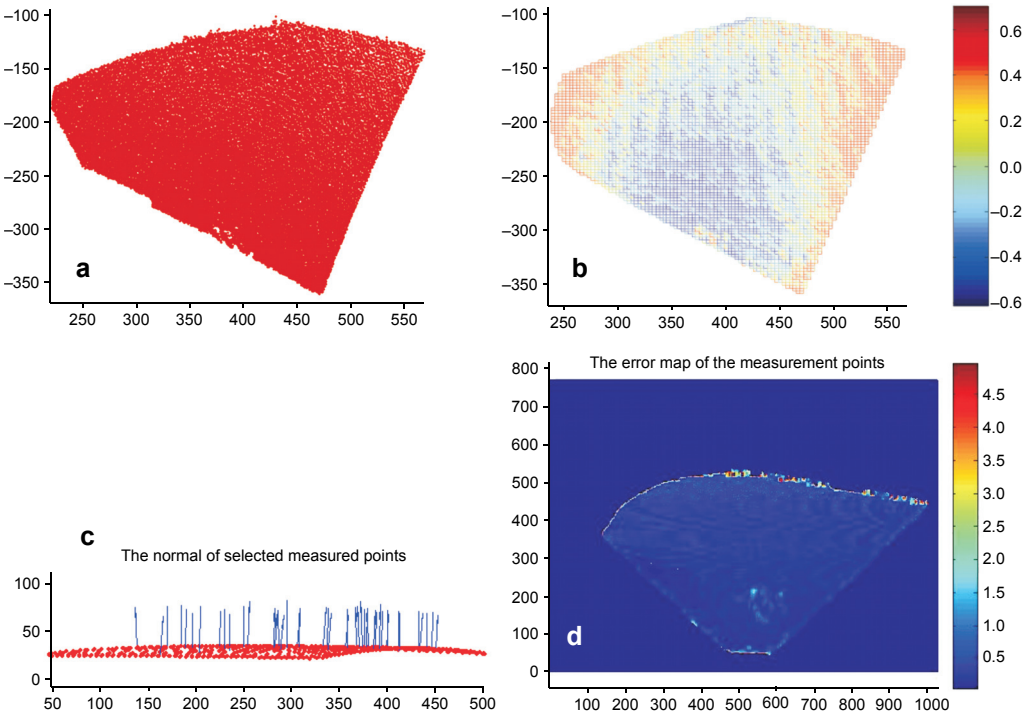

Fig. 12. The experimental result for automotive glass: point cloud (**a**), error map (**b**), surface normal (**c**), transmission distortion (**d**).

is also obtained, as shown in Fig. 12**c**. The surface normal denotes the reflection property of the glass. The transmission distortion is shown in Fig. 12**d**. The unit of the transmission distortion is degrees (in the color bar).

Last, the different methods for 3D shape inspection are compared, including: CMM, diffuse object inspection system developed in our lab [15], transparent object inspection system proposed in the paper.

As shown in the Table, the CMM inspection method is time consuming. The operator needs to measure the windshield point-by-point; the inspection speed depends on the operator's skills. The time cost of specular method is less than that of diffuse one because diffuse strategy needs spraying the windshield. The CMM method has very high accuracy but low resolution performance. The diffuse and specular methods have similar performance as regards accuracy and resolution. Most

T a b l e. Comparison of different inspection methods.

Method	Time	Accuracy	Resolution	Optical property
CMM	30 s/point	0.1 μm	Low	No
Diffuse	60 s	0.18 mm	High	No
Transparent	40 s	0.25 mm	High	Yes

importantly, the method proposed in this paper can obtain the optical property of the glass, including reflection normal and transmission distortion.

4. Conclusions

In this paper, an integrated inspection system for automotive glass is proposed. Not only the 3D shape, but also the optical property of the automotive glass, including the reflection normal and transmission distortion are measured in our inspection system. The principle of the inspection system is based on analyzing the distorted fringe patterns. The reflection law of the automotive glass is considered as the criterion for solving the correspondence problem of the stereo vision. Additionally, the GCLS fringe pattern is adopted to solve the problem of the bottom reflection. Then, the 3D shape and surface normal of the automotive glass are obtained. Compared with the phase distribution of the reference, the angle of transmission distortion is determined for quality inspection. Last, the experimental results demonstrate that the method proposed for transmission distortion of the automotive glass is very simple and efficient.

Reference

[1] PETRIU E.M., SAKR Z., SPOELDER H.J.W., MOICA A., *Object recognition using pseudo-random color encoded structured light*, Proceedings of the 17th IEEE Instrumentation and Measurement Technology Conference, May1–4, 2000, Baltimore, Maryland, USA, pp. 1237–1241.

[2] CHI ZHANG, NING XI, QUAN SHI, *Object-orientated registration method for surface inspection of automotive windshields*, IEEE/RSJ International Conference on Intelligent Robots and Systems (IROS), September 22–26, 2008, Nice, France, pp. 3553–3558.

[3] ZHENG J.Y., FUKAGAWA Y., ABE N., *3D surface estimation and model construction from specular motion in image sequences*, IEEE Transactions on Pattern Analysis and Machine Intelligence **19**(5), 1997, pp. 513–520.

[4] SKYDAN O.A., LALOR M.J., BURTON D.R., *3D shape measurement of automotive glass by using a fringe reflection technique*, Measurement Science and Technology **18**(1), 2007, pp. 106–114.

[5] HOROVITZ I., KIRYATI N., *Depth from gradient fields and control points: Bias correction in photometric stereo*, Image and Vision Computing **22**(9), 2004, pp. 681–694.

[6] HONGWEI GUO, PENG FENG, TAO TAO, *Specular surface measurement by using least squares light tracking technique*, Optics and Lasers in Engineering **48**(2), 2010, pp. 166–171.

[7] DIN 52305 – STANDARD, *Determining the optical distortion and refractive power of safety glazing material for road vehicles*, 1995.

[8] MASI C.G., *Moiré interferometry spots windshield defects*, Image Processing Europe **5**(6), 2002, pp. 22–25.

[9] PETZ M., TUTSCH R., *Reflection grating photogrammetry: A technique for absolute shape measurement of specular free-form surfaces*, Proceedings of SPIE **5869**, 2005, p. 58691D.

[10] KNAUER M.C., KAMINSKI J., HAUSLER G., *Phase measuring deflectometry: A new approach to measure specular free-form surfaces*, Proceedings of SPIE **5457**, 2004, pp. 366–376.

[11] HARTLEY R., ZISSERMAN A., *Multiple View Geometry in Computer Vision*, 2nd Edition, Cambridge University Press, Cambridge, 2003, pp. 239–259.

[12] XIANZHU ZHANG, NORTH W.P.T., *Analysis of 3-D surface waviness on standard artifacts by retroreflective metrology*, Optical Engineering **39**(1), 2000, pp. 183–186.

[13] FISHER R.B., NAIDU D.K., *A comparison of algorithms for subpixel peak detection*, [In] *Image Technology: Advances in Image Processing, Multimedia and Machine Vision*, Springer, Berlin, Heidelberg, New York, 1996, pp. 385–404.

[14] ZHANG Z., *A flexible new technique for camera calibration*, IEEE Transactions on Pattern Analysis and Machine Intelligence **22**(11), 2000, pp. 1330–1334.

[15] CHI ZHANG, NING XI, JING XU, *et al*., *Calibration of a structure light based windshield inspection system*, IEEE International Conference on Robotics and Automation (ICRA), May 3–8, 2010, Anchorage, Alaska, USA (in press).

Received October 27, 2009
in revised form February 17, 2010